Spectral phasor plot for hyperspectral imaging of acridine orange photophysics within the cell

Marcela Díaz[1], Flavio R. Zolessi[1,2], Leonel Malacrida[1,3*]
[1]Unidad de Bioimagenología Avanzada, Institut Pasteur de Montevideo - Hospital de Clínicas Universidad de la República.
[2]Sección Biología Celular, Facultad de Ciencias, Universidad de la República.
[3]Departamento de Fisiopatología, Hospital de Clínicas, Universidad de la República.
***Correspondence to: lmalacrida@pasteur.edu.uy**

Keywords: Acridine Orange, RNA, fluorescence microscopy, hyperspectral imaging, phasor analysis.

Abstract

Acridine Orange (AO) has rich photophysics that has been exploited to study its interaction with RNA and DNA. Traditionally AO was used to stain cells differentiating nucleus and cytoplasm due to the differences in DNA and RNA differential composition. AO cell labeling shows complex behavior depending on several parameters, such as concentration, pH, etc. Such complex photophysics will benefit from a model-free analysis such as the spectral phasor (SP) for hyperspectral imaging. The SP linear combination and reciprocity principles allow us to understand better the AO spectral shift associated with its exploration of the different molecular environments in cells. Using this approach, we identified the SP fingerprints for RNA and DNA for in vitro experiments, which remain invariant for fixed and live cells. However, the SP analysis of the AO fluorescence from live cells shows the occurrence of a third spectral component at 640 nm. The linear properties of the SP analysis enable quantification of the AO bound to RNA, DNA, and a third component. By co-labeling with AO and LysoTracker, we associated part of these subcellular structures with acidic compartments. Nonetheless, we could differentiate AO self-interactions from its binding to RNA within cytoplasmic compartments by use of the SP analysis. This work establishes the use of SP for hyperspectral imaging of AO for the first time, expanding our knowledge of its complex photophysics and promoting further application for in vivo cell imaging.

1. Introduction

Acridine orange (AO) is a cationic dye that has unique photophysics properties. Various uses of this molecule are described in the literature, and the spectral properties seems to vary depending on its concentration, charge, and the nature of the molecules that surround it [1], [4]. AO in aqueous solution could stay in two forms: at low concentrations (below 10^{-5} M), where monomers predominate, the maximum absorption peak of AO is at 490-494 nm and emission is at 530 nm. However, AO in concentrated solutions (more than 10^{-2} M) stays in a dimer form with an absorption maximum at 465-467 nm and emitting red fluorescence at 640 nm [2], [3], [5].

Since the first studies in 1940, where AO fluorescence was used to label cell nuclei in living and dead plant cells, metachromatic changes were visualized when this dye differentially interacts with single or double stranded nucleic acids [2], [4], [6], [7]. When AO interacts with double stranded (*ds*) DNA or RNA in a low ratio of AO to nucleic acid, an A-type complex is formed and monomeric AO molecules are intercalated between the base pairs. These complexes have an absorption maximum at 503 nm and green fluorescence with a maximum peak at 530 nm. On the other hand, AO interacting with single stranded (*ss*) regions of RNA and denatured DNA can form B-type complexes. This type of complex is characterized by absorption at 475 nm and by emission of red fluorescence with a maximum peak at 640 nm [2]. In this case, dye-dye interactions are generated through the binding with the phosphate backbone of nucleic acids in a process known as “stacking”, which involves the formation of polymeric stacking of dimers generating multimers [1], [4], [8]. At very high concentrations, RNA binding sites are saturated with AO, and aggregation of molecular complexes can occur, resulting in the precipitation of solid aggregates with red fluorescence [6], [9].

Under highly controlled conditions of pH and concentration, AO is useful as a good cytochemical probe for nucleic acid labelling in fixed cells, resulting in green fluorescence from the nucleus (DNA) and red homogeneous fluorescence from cytoplasm and nucleoli (RNA) [2]. When using a low concentration of AO (5×10^{-6} M), the labeling pattern on living cells differs from that obtained on fixed cells [2]. In living cells, a bright green nucleus and nucleoli can be distinguished, while the presence of red cytoplasmic granules is the most conspicuous feature [2]. These structures have already been reported since 1944, and in these first studies were related to complexes formed between AO and cytoplasmic RNA. However, in the 1960s that idea was discarded, and

these red cytoplasmic granules were identified as lysosomes and other acidic compartments [2], [7], [8], [10]. Reports indicate that AO labels cytoplasmic acidic compartments not solely due to the low pH, but rather due to the elevated concentration of this dye within these organelles [7], [10]. The mechanism of dye accumulation in these vesicles is an energy-dependent process that involves protonation in a low pH environment, preventing AO molecules from crossing the vesicular membrane again and trapping them in these acidic spaces [2], [7]. As the concentration of AO rises, it leads to the formation of aggregates in the form of dimers and excimers, which subsequently generates a red metachromatic shift. [2], [5], [10], [11].

Plemel et al., [9] collaborators demonstrated that MO3 cells stained with 200 µM AO exhibit distinct spectral characteristics in the nucleus (peak at 530 nm) and cytoplasm (red peak at 650 nm). To the best of our current knowledge, this is the only report that exploits hyperspectral imaging to explore the spectral characteristics of AO specifically for studying living cells. Traditional analysis of AO spectral imaging allows a limited comprehension of spectral changes associated with this dye interacting other molecules [9].

The Spectral Phasor Plot (SP) for hyperspectral imaging is a method based on the Fourier transform, where spectra of individual pixels in an image are represented in a polar plot (real and imaginary components of the Fourier transformation) [12][13]. The SP is a straightforward tool that can provide a model-free analysis of AO complex photophysics upon its interactions with different subcellular environments. Based in its simple rules, such as the linear combination and reciprocity principle, the SP enables to identify the occurrence of different molecular environments for a dye of interest with no previous knowledge[14]. In the past, this approach has been used to understand the photophysics of LAURDAN or ACDAN in various systems such as cell, plants or animals [15][12][16] . Using this approach, one can take full advantage of the hyperspectral imaging for live cell experiments [17][18][19][20][21].

In this study, we used hyperspectral confocal microscopy and spectral phasor analysis to assess the unique metachromatic properties of AO interacting with nucleic acids (RNA and DNA) and also exploring various subcellular compartments *in vitro* and *in vivo*. We successfully untangled the molecular environments for AO in cells, and due to the

unique model-free approach of SP, it was possible to decipher the molecular entity for the red-shifted fluorescence of AO. This environment resulted from its self-interaction and its binding to RNA within cytoplasmic compartments. Using hyperspectral imaging and spectral phasor opens further methods of investigations for RNA and DNA *in vivo*.

2. Materials and methods

2.1. Dyes and Reagents

The dyes and dilutions employed in this work were: Acridine Orange hemi (zinc chloride) salt (AO, 27 mM stock solution in DMSO; 50 µM work dilution, in PBS for DNA/RNA solutions and fixed cells, in cell culture medium for *in vivo* cell experiments; Sigma-Aldrich #A6014), LysoTracker™ Deep Red (0.3 µM in cell culture medium for in vivo staining; ThermoFisher, #L12492). For cellular fixation, we used 4 % Paraformaldehyde in PBS (Sigma-Aldrich #158127) and for permeabilization Triton™ X-100, 0.1 % in PBS (Sigma-Aldrich #x100). UltraPure Salmon Sperm DNA solution (0.1 and 10 mg/mL; ThermoFisher #15632011). RNA from yeast diluted in PBS (0.7 and 2 mg/mL; Sigma-Aldrich, Merck #10109223001).

2.2. AO bound to DNA or RNA

AO was mixed with an ultra-pure DNA solution or RNA from yeast diluted in PBS for a final AO concentration of 50 µM. Concentrations at which AO is fully bound to nucleic acids were determined by evaluation of various solutions. The amount of dye versus DNA or RNA was optimized considering signal to noise of AO and the spectral phasor plot shift toward the blue (increase in AO bound).

2.3. Cell culturing

NIH-3T3 cells (ATCC #CRL-1658™) were cultured in DMEM with GlutaMAX (ThermoFisher, #10566016), supplemented with 10% Donor Bovine Serum (ThermoFisher #16030-074), HEPES (10 mM; ThermoFisher, #15630080) and penicillin-streptomycin (100 U/mL; ThermoFisher #15140122). Cells were maintained under a 5 % CO_2 atmosphere and at 37 °C. For sub-culture we used Trypsin with 0.25 % EDTA (ThermoFisher, #25300054).

One day before imaging, cells were seeded onto 35 mm glass-bottom Petri dishes (Greiner Bio-One, #627870) at a density of $2.5x10^5$ cells per dish.

2.4. Cell staining

- NIH-3T3 live cells

Staining with AO was performed through incubation of the cells with the indicated concentration diluted in cell culture medium for 10 min at 37 °C. Before imaging, the cells were washed with a medium change. In LysoTracker™ Deep Red experiments, cells were incubated first with this dye for 10 min at 37 °C; after a wash with cell medium, confocal images were acquired. Second, AO was added to the medium, washed with cell medium and new confocal images were acquired.

- Fixed NIH-3T3 cells

Cells were fixed for 10 min in 4 % PFA, and washed 2x in PBS with 0.1 % Triton X100. For staining, cells were incubated with the indicated concentration of AO diluted in PBS for 10 min before acquiring images under the microscope.

2.5. Confocal microscopy and hyperspectral imaging

All spectral images were obtained using a confocal microscope Zeiss LSM 880 equipped with 63x oil immersion lens (NA 1.4, Plan Apochromat, DIC M27, Zeiss) and using the lambda mode on the Zen black v. 2.3 software (Zeiss). For excitation we used 488 nm Argon laser (AO) and 633 nm diode laser (LysoTracker Deep Red). In this last case, we used a multiband pass dichroic mirror MBS 488/561/633. Emission spectra acquisition was done using a spectral detector (gallium arsenide phosphide photomultiplier tube; GaAsP-PMT), capturing 22 consecutive steps (channels). Spectral images of 256 x 256 pixels were acquired with 10 nm steps, covering the spectral range from 503 to 723 nm. For AO solutions with nucleic acids, a drop of 30 µL was placed on a coverslip and imaged by spectral confocal microscopy. Excitation was set at 488 nm, using the MBS 488 dichroic. Spectral images of 256 x 256 pixels were acquired with 10 nm resolution, covering the range of 503 to 723 nm. Pixel dwell time used was 0.67 µs/pixel, and a line average of 2 was used.

For cell imaging with emission detection in two channels, we used a 488 nm Argon laser: green fluorescence (500 to 582 nm) and red fluorescence (583 to 630 nm); a MBS 488 dichroic mirror was used. When LysoTracker Deep Red was evaluated, excitation was done using 633 nm diode laser and acquiring a third emission channel from 698 to 740 nm. In this case, we selected the MBS 488/561/633 dichroic mirror. Frame sizes of 512 x 512 pixels were acquired with 10 nm resolution covering the range of 503 to 723 nm. During live cell imaging, controlled atmospheric conditions were maintained: 37 °C and 5 % CO_2. All images were obtained using a pixel size between 130 and 100 nm, and the pixel dwell time used was 0.85 µs/pixel.

2.6. Image processing

Brightness and contrast, smooth filter, sum of lambda channels for the generation of stack images, and placement of scale bar were done using Fiji software [22]. The tool *plot z axis* from Fiji was used to make the basic spectral analysis of the ROIs selected in the hyperspectral images of fixed and live cells. The ROIs were placed in the nucleus and cytoplasm seeking to observe cellular regions that on average have a higher proportion of DNA (nucleus) or RNA (cytoplasm). The color scale for lambda channels was obtained from Zeiss 2.3 Zen black software.

- Spectral phasor plot analysis and interpretation

For hyperspectral data analysis, we used the spectral phasor transformation using SimFCS software (G-Soft, Illinois-USA) developed at the Laboratory for Fluorescence Dynamics (www.lfd.uci.edu). Through this approach, based on the Fourier transform, data of each pixel of spectral images is processed as described previously by [20]. The spectral phasor transform is defined as:

$$x = G_{(\lambda)} = \frac{\int_{\lambda min}^{\lambda max} I_{(\lambda)} \cos\left(\frac{2\pi n(\lambda-\lambda min)}{\lambda max-\lambda min}\right) d\lambda}{\int_{\lambda min}^{\lambda max} I_{(\lambda)} d\lambda} \text{ (eq. 1)}$$

$$y = S_{(\lambda)} = \frac{\int_{\lambda min}^{\lambda max} I_{(\lambda)} \sin\left(\frac{2\pi n(\lambda-\lambda min)}{\lambda max-\lambda min}\right) d\lambda}{\int_{\lambda min}^{\lambda max} I_{(\lambda)} d\lambda} \text{ (eq.2)}$$

I(λ) is the intensity at each step in a spectral range λmax to λmin, n the harmonic number (1 in our case), λmin is the initial wavelength. Values of G and S are assigned to each pixel in the images and located in the spectral phasor plot. SimFCS software calculates a 2D phasor plot and an average intensity image (from the 32-channel spectral image). In the phasor plot, spectral data is represented as a cloud, whereas the heat map shows the accumulation of pixels. The connection between real and imaginary space can be exploited using cursors in the phasor plot. By doing so, one can interactively understand the fluorescent components presented in the sample.

The position at the phasor plot depends on the spectrum shape, where spectrum center of mass is captured by the phase angle (θ), and the spectrum width by the modulation vector (M). Spectral shift to longer wavelengths implies increasing phase angle and a spectrum broadening moves the position toward the center (M decreases). One of the most significant properties of the phasor plots is the use of the vector properties, such as the linear combination and the reciprocity principle. The linear combination allows the study of multiple components in a mixture as a sum of fractions of single components. Thus, the position of a combination of two spectrums is located on the line that connects the two pure components [20]**.** The reciprocity principle allows for the selection of a region of interest (ROI, or cursors) on the phasor plot and identifies the corresponding pixels in the average intensity. Additionally, this phasor property also operates in reverse by drawing an ROI on the original image and obtaining the associated phasor plot. We utilized this property to map the AO spectral properties within the cellular environments by masking nuclear or cytoplasmic ROIs. The Phasor plot enables the use of a median filter (3x3 kernel) to improve signal to noise; using SimFCS software we applied such filter for all our phasor analyses.

For fixed or live cells experiments, we defined two or three cursors based on phasor position from pure components. For fixed cells, a two components analysis was done using the SimFCS software. To quantify the amount of each component at the image, we calculated the component fraction histograms [23]. We determined the fraction of AO bound to DNA (cursors 1) or to RNA bound, counting the number of pixels between the linear combination that joins the two pure components.

For live cells, we used the three components analysis developed by Ranjit et al., [24], we quantified the fraction of DNA-bound AO, or the third component (C_3) and its subcellular distribution using the addition rules of phasor plots. Through the segmentation tool of SimFCS software, we segmented individual cells from images and separated nuclei from cytoplasm. Then, a quantitative analysis was made obtaining the contributions of each AO component through fractional histograms. In this representation the number of pixels at each position in the plot is represented along the line or trajectory DNA-RNA and DNA-C_3, normalized by the total fraction. Then, we could plot the mean value and standard deviation for each histogram.

For a statistical comparison between different groups, we calculated the Center of mass (CM) for the AO fraction histogram bound to DNA or C_3. The CM was calculated as following:

$$CM = \frac{\sum b.f(x)}{\sum f(x)} \text{ (eq. 3)}$$

with 'b' being the percentage of pixels at the fraction 'f(x)' of the variable 'x' namely AO-DNA fraction or AO-C_3 fraction [12].

2.7. Statistical analysis

Three independent biological replicates were used to validate this work. For statistical analysis, 10 images were acquired per condition. For the analysis, individual cells stained with AO were segmented by hand drawing: 15 live cells and 12 fixed cells. Mean curves for fraction histograms were shown as mean ± standard deviation. Center of mass plots were shown as median value for each condition with the dispersion of the data. We use the Violin plot as the method to compare results; the design was generated through PlotsOfData, a web app for visualizing data together with their summaries [25]. The analyzed samples showed no normal distributions. Therefore, the Wilcoxon matched-pairs test was used to study the non-parametric data. In the case of the violin plots of fixed cells $p=0.0005$, for the living cells $p<0.0001$ was considered statistically significant. Statistical analysis was performed using GraphPad Software, Inc.

3. Results

To evaluate the interaction of AO with DNA and RNA, hyperspectral microscopy images of DNA or RNA PBS solutions mixed with 50 µM AO were performed. By titrating nucleic acids solutions with increase concentrations and constant AO, it was possible to identify a spectral phasor plot (SP) where there was no further change in the center of mass of the phasor position. This ratio was at 10 mg/ml for DNA and 2 mg/ml for RNA. As shown in figure 1A, the cyan, green, and magenta cursors were positioned around the center of mass of each phasor cloud. According to these results, AO undergoes spectral changes associated with its interactions with nucleic acids. The spectrum is shifted towards shorter wavelengths in both cases (smaller phase) compared to free AO. Using cursor selection, pseudo-color images were prepared (figure 1B), showing homogeneous images, indicative of the absence of aggregation. Notice that spectral plots, fluorescence intensity vs. wavelength, obtained after titration of AO bound to DNA or RNA, show a maximum emission peak near 540 nm. While free AO or bound to DNA or RNA shows similar spectra, the phasor plots capture the shape changes and the positions in the SP are different (figure 1A and B).

As represented in figures 1C and D, the SP plots for solutions with intermediate concentrations of DNA (0.1 mg/ml) or RNA (0.7 mg/ml) (partial binding of AO to nucleic acids) fall into the linear combination between free AO and DNA or RNA bound. The fraction histograms (figure 1C and D, right panels) show the different samples tested for free AO, partially bound to DNA or RNA, and fully bound to DNA and RNA. Notice that by using the fraction histogram we can quantify the different fraction of free or bound AO.

Hyperspectral images of AO-stained fixed cells (50 µM AO, washed after fixation with PBS-Triton X100 and leaving free AO during the image acquisition) enables the identification of cytoplasmic and nuclear structures, including nucleoli, due to the changes in AO brightness (figure 2A). Examining the average spectrum (fluorescence intensity as a function of wavelength) from nuclear and cytoplasmic ROIs shows subtle differences in AO fluorescence (fig. 2A. On the other hand, phasor plot analyses of the

fixed cell hyperspectral images (figure 2B) shows a cloud on top of the fixed cursors, which were previously assigned for AO fully bound to DNA and RNA (figure 1). The pseudo-color image of Figure 2B demonstrates the distribution of AO bound to DNA (green pixels) or RNA (magenta pixels) in the segmented cell. Notice that the cell nucleus shows a greater fraction of pixels coming from AO interacting with DNA, while in the cytoplasm there is a higher proportion of RNA-bound AO.

Quantitative analysis of the AO fluorescence by the SP analysis in fixed cells is presented in Figure 3. The representative pseudo-color image indicates regions with higher proportion of DNA-bound AO in the nucleus (red) (see figure 3A). Notice, nucleoli inside the nucleus are characterized by greenish/blueish pixels, which correspond to higher proportions of RNA-bound AO. At the cytoplasmic level, there is a greater proportion of RNA-bound AO.

Figure 3B shows the histogram of DNA-bound AO fraction. Ten hyperspectral images of whole cells were analyzed; results show that cells present 50% of pixels with equal proportions of AO bound to DNA and RNA. Note that the black curve represents the average and standard deviation. Masking analysis of the cells were performed to study the nucleus and cytoplasm regions independently (figure 3C and D, respectively). The nucleus masking identifies an increased fraction towards the AO-DNA component (see zoomed area of the SP, figure 3C). This result is confirmed by looking at the DNA-bound AO fraction histogram, see right panel figure 3C. The component fraction histogram shows a ratio of 65 % AO-DNA to 35 % AO-RNA; see the average curve of this (black curve). The SP analysis of the cytoplasmic masking shows a displacement of the center of mass of the cluster towards the AO-RNA component (figure 3D). This result is shown by a higher proportion of blue pixels in the pseudo-color image of the cytoplasm; see the inset in figure 3D. Quantification of the fraction histogram of DNA-bound AO indicates an average of 40 % AO-DNA and 60 % RNA-AO. Notice, the fixed cells analyzed show a narrow variability on its DNA-RNA AO fraction (fig. 3D right). Figure 3E shows the nucleus and cytoplasm distribution of the centers of mass for the DNA-bound AO fraction histograms represented as a violin plot. Thus, we were able to determine a significant difference with a lower proportion of DNA-bound AO in the cytoplasm versus the cell nucleus ($n=10$, $p=0.0005$).

Next, we study the AO fluorescence in living cells, where it is possible to observe that the nucleus exhibits a green fluorescence with its perimeter well marked, and a nucleolus intensely marked with green fluorescence. The green component is very weak in the cytoplasm, while several small granules are distinguished with an intense red fluorescence (figure 4A). The average spectrum at two ROIs associated with the nucleus and cytoplasm shows the occurrence of cytoplasmic AO red particulates in living cells. Here, in addition to the 540 nm peak, a second emission peak is observed in the spectral plot centered at 640 nm (figure 4A right). To better appreciate what subcellular structures are associated with these spectral changes, we divided the hyperspectral image into two sub-images. Image 1 is formed by the average intensity of channels between 503 and 583 nm, and image 2 between 603 and 723 nm (figure 4B). In image 1, an intense nuclear signal predominates, moreover, a nuclear perimeter and nucleoli are distinguished (see figure 4B left panel). On the other hand, image 2 highlights the occurrence of small perinuclear cytoplasmic structures; note that these structures are not visible in image 1 (figure 4B central panel). Then we analyzed the same data using the SP approach. The SP plot identified three components (figure 4C). Using cursors, the AO fluorescent components were highlighted on the plot with magenta and green cursors, for RNA and DNA bound AO (figure 4C), respectively. The position for these components is the same reported in Figure 2 for fixed cells. In addition, the results show the existence of a third component for AO (C_3) in living cells. The C_3 is marked in figure 4C (central panel) by a cyan rectangle. The pseudo-color image in figure 4C (right panel) shows a distribution of DNA-bound AO mostly at the nuclear level and RNA-bound AO in nucleolus and cytoplasm. The C_3 shows a perinuclear distribution associated with the red cytoplasmic particles that were visible in the hyperspectral images (figure 4A).

By using the phasor plots three-components analysis we were able to determine the distribution of the DNA/RNA AO fraction in the presence of a third component. The analysis of the dimension of AO interacting with DNA and RNA/C_3, represented with a color scale from red to blue in figure 5A, shows a higher fraction of DNA-bound AO at the nucleus. While the perinuclear region at the cytoplasm shows an increased fraction of RNA-bound AO pixels. In the nucleoli, we can observe intermediate proportions of the components indicated by the yellow color scale. Notice the heterogeneous distribution obtained in the AO-DNA fraction histogram from the various cells analyzed

(figure 5B, top panel). The average curve shows 80-90 % of DNA-bound AO for live cells. By masking the nuclei, the cell variability on the fraction of AO bound to DNA or RNA was preserved (figure 5C). The center of mass for the AO-DNA fraction histogram (Figure 5E, upper panel), demonstrates a strong cell to cell variability, with a higher proportion of DNA-bound AO in the nuclei than in the cytoplasm. On the other hand, when analyzing the trajectory of DNA/RNA bound AO or with the third component, it is clear that C_3 is only found at the cytoplasm (pseudo-color image in 5A below and figure 5D). This result can be confirmed by looking at the phasor plot of segmented nucleus, where there are no data showing linear combinations with C_3 (figure 5C). Furthermore, the violin plot in figure 5E (bottom panel), shows a significantly higher fraction of AO-C_3 in the cytoplasm than in the nucleus, where it is virtually absent (median 12 %, $p<0.0001$).

To further investigate the nature of the AO third component in living cells we exploited the linear combination properties of SP introducing a fluorescent marker for acidic-like organelles. We co-labeled living cells with AO and LysoTracker Deep Red (Figure 6A to E). Although AO marks acidic compartments in living cells, not all AO-positive cytoplasmic structures were acidic-like organelles. The LysoTracker Deep Red appears at the SP plot in the fourth quadrant, enabling the combination with the AO three components described before (figure 6F). The cell co-stained with AO and LysoTracker Deep Red shows a complex SP distribution due to the linear combinations with four components, namely AO bound to DNA, RNA, C_3 and LysoTracker Deep Red (figure 6G). Two clusters can be identified, the magenta which is associated to the C_3 component. While the yellow area contains the pixels that are linear combinations of LysoTracker Deep Red with C_3 and RNA/DNA bound AO. This cluster is indicative of the acidic organelles' characteristic of some of the subcellular organelles labeled by AO, while a percentage stays at the linear combination between RNA/DNA and C_3. The existence of two different populations of subcellular structures is evidenced in the pseudo-color inserted image of figure 6G.

4. Discussion

The interaction of AO with nucleic acids *in vitro* is well known and has been characterized from spectroscopic to molecular points of view [9], [26], [27]. The spectral changes associated with the AO interaction with itself or with nucleic acids (DNA and RNA) is useful to differentiate qualitatively and semi-quantitatively sub-cellular structures in living and fixed cells. In the present work, we aimed to revise AO fluorescence from cells using the unique model-free approach of the spectral phasor analysis of hyperspectral imaging. This method proved sensitive to the various AO environments in cells, identifying several sub-cellular compartments and providing a comprehensive understanding of the AO molecular interaction in the cell.

The spectral shifts experienced by AO bound to RNA or DNA are similar in their spectrum maximum and shape, which complicates unmixing and quantification (figure 1B, lower panel). However, SP analysis of AO hyperspectral imaging shows an unequivocal position at the phasor plot due to the molecular environments offered by DNA or RNA. When AO interacts with RNA, the cloud of data in the SP shows a longer phase (redder spectrum) than when interacting with DNA. This spectral shift can be associated with the AO diverse types of interactions with nucleic acids, such as single-strand (ss) or double-strand (*ds*), base pairs intercalation, monomers, and stacking with dimer formation [8], [27], [28]. To better understand if we can distinguish in the phasor space between *ss* and *ds* nucleic acids, further *in vitro* studies with AO solutions and purified *ss*/*ds* DNA and RNA were necessary. Using this approach, we identified the coordinates corresponding to these molecular environments that supports the unique SP fingerprints.

Solutions of AO with various concentrations of nucleic acids were analyzed by SP. Figure 1C and D shows examples of the clusters obtained from solutions with different fractions of free AO, and DNA or RNA bound AO (full bound). The results show that solutions containing free and bound AO lie on the line between the pure components, illustrating the linear combination principle of phasor plots. The importance of a model-free approach, such as the phasor plot, is highlighted here because the phasor position for AO in vitro and in cells overlaps. This fact enables us to stand on a robust analysis for our cellular studies, since the spectroscopic properties of AO bound to RNA or DNA identifies a molecular location that remains invariant at the phasor plot.

According to Plemel et al., a 140 ng/µl RNA solution with 50 µM AO is sufficient for the formation of an AO-RNA complex that shows a peak around 640 nm [9]. Our experiments did not indicate this spectral shoulder, even with higher RNA concentrations (2 µg/µl). This discrepancy could be explained due to the different excitation wavelength used. We chose 488 nm excitation considering the several previous reports of AO spectral analysis using living and fixed cells [2], [4], [9], [29]. Excitation wavelength may modify the emission profile by the preferential selection of an AO specific ground state. For example, Plemel et al., excited *in vitro* solutions at using 457 nm light, however, for fixed cells they used 488 nm excitation [9]. The 457 nm excitation preferentially excite AO dimeric forms (absorption at 465 nm), and the possible B-type complexes that are formed when AO interacts with single-stranded RNA (absorption at 475nm) [2]. Other variables that can influence the spectral shift towards the second peak in red wavelengths. For instance, the time variable can favor complex molecular interaction, another very sensitive variable is the dye to solute concentration. According to Kapuscinski et al. the formation of AO solid complexes with RNA could take time (at least 24 hours), and thus a precipitate is formed that fluoresces at 650 nm [6].

AO-stained NIH-3T3 fixed cells show a homogeneous spectral profile with subtle differences between nuclear and cytoplasmic regions (figure 2A). This result appears to be contradictory with the observations previously reported in the literature, where cells fixed and stained with AO show a pattern of green fluorescent nuclei, yellow nucleoli and red cytoplasm. [2], [4], [9]. We consider that this difference can be assigned to the methodological conditions used in the present work. The use of Triton X100 after fixation facilitates the loss of the red spectral component. Under these experimental conditions the ability of the SP to differentiate molecular environments for RNA and DNA bound AO is demonstrated (Figure 2B).

The SP analysis of AO hyperspectral images in living cells further demonstrates the power of this approach. Without assuming any a priori model and while only visualizing the data in the frequency space of the phasor plots, we were able to evidence the presence of third AO molecular environments (figure 4C, central panel). An interesting aspect of discussing this result is the variability of the RNA/DNA bound AO or C_3 obtained within the group of cells analyzed (figure 5C, D, and E). One can speculate with the different cell cycle stadiums of the cell, considering the culture was not synchronized.

This analysis could be an interesting application for AO uses on live cell images and was previously exploited to identify apoptosis in fixed experiments [9].

C_3 is present in the perinuclear region of the cytoplasm, and the SP shows a linear trajectory from the RNA and DNA position toward the C_3, indicating different fractions of this component with the others (figure 4C). According to previous work, AO can accumulate in acidic compartments of living cells undergoing a metachromatic change[2], [10], [4], [8]. These results seem to show the well-studied interaction of AO with organelles like lysosomes [6], [9], [10], [27], [28], [30]. AO in these cellular environments can form multimers, such as dimers and excimers that fluoresce with a peak at 640 nm [5], [11], [31]. To study the nature of C_3-positive granules, and evidence if they correspond to acidic subcellular compartments, we co-labeled living cells with LysoTracker Deep Red and AO. The selection of this fluorophore relies on its excitation around 633 nm, thus no excitation of AO was observed. Adding this extra component dragged some of the pixels from the RNA-C_3 linear combination, indicating that part of the C_3-positive perinuclear cytoplasmic granules were acidic (yellow cluster in figure 6C). Interestingly, not all the C_3 positive pixels were labeled by LysoTracker Deep Red, evidencing a variety of AO-stained granules. These vesicles shown different proportions of RNA-bound AO. Therefore, we hypothesize that the C_3 component could be related to the occurrence of stacking and B-type complexes for AO due to different RNA/dye concentrations in diverse cytoplasmic RNA-containing structures. These organelles could be stress granules, processing bodies, ribosomes and extracellular vesicles as exosomes that interact with RNA [32]–[34].

5. Conclusion

Overall, SP analysis of AO hyperspectral data is shown to be a very sensitive tool that allowed us to study in detail the complex photophysics of AO within different sub-cellular compartments. Using this approach, we analyzed DNA/RNA AO-bound fractions quantitatively. The AO SP profile was different for fixed and live cells. On live cells, a third environment was distinguished and associated with the 640 nm AO peak, which we associate with a fraction of acidic organelles. However, part of these organelles remains elusive in their identity opening the opportunity for further investigation. SP analysis of AO hyperspectral imaging is a better tool than the classical method of

radiometric or emission spectra evaluation, enabling one to differentiate acidic compartments (where AO forms multimers) from cytoplasmic structures where AO interacts with RNA. Combining AO staining on fixed or live samples with the SP approach, a powerful method is formed, allowing for a quick and easy analysis of complex data on the sub-cellular organization of different biological subjects, from cells to tissues.

Acknowledgments

The authors declare no conflict of interests. The authors would like to thank the Advanced Bioimaging Unit-Institut Pasteur of Montevideo-HC Udelar. LM is supported by the grants 2020-225439, 2021-240122, 2022-252604 of Chan Zuckerberg Initiative DAF, an advised fund of Silicon Valley Community Foundation. LM, MD and FZ were supported by FOCEM - Fondo para la Convergencia Estructural del Mercosur (COF 03/11). FZ and LM thanks PEDECIBA for their support as investigators of the post-degree program.

Data availability statement

The data that support the findings of this study are openly available at the following URL/DOI: https://doi.org/10.6084/m9.figshare.23656989.v1

ORCID iDs

Marcela Díaz https://orcid.org/0000-0002-5130-0287

Flavio R. Zolessi https://orcid.org/0000-0003-2405-994X

Leonel Malacrida https://orcid.org/0000-0001-6253-9229

References

[1] J. W. Macinnes and R. B. Uretz, “Spectral Analysis of the Binding of Acridine Orange to Polytene Chromosomes,” *PNAS*, vol. 55, no. 5, pp. 1109–1113, 1966.

[2] A. V Zelenin, “Chapter nine - Acridine Orange as a Probe for Cell and Molecular Biology,” *Biol. Tech. Ser.*, pp. 117–135, 1999, doi: 10.1016/B978-0-12-447836-7.50011-7.

[3] A. M. Amado *et al.*, “The effect of dimethylsulfoxide on absorption and

fluorescence spectra of aqueous solutions of acridine orange base," *Spectrochim. Acta - Part A Mol. Biomol. Spectrosc.*, vol. 22, no. 1, pp. 943–949, 2019, doi: 10.1016/j.saa.2015.06.126.

[4] F. H. Kasten, "Introduction to Fluorescent Probes: Properties, History and Applications," *Fluoresc. Lumin. Probes Biol. Act.*, pp. 17–39, 1999, doi: 10.1016/b978-012447836-7/50004-x.

[5] I. G. Shenderovich, "The Partner Does Matter: The Structure of Heteroaggregates of Acridine Orange in Water," *Molecules*, vol. 24, no. 15, 2019, doi: 10.3390/molecules24152816.

[6] J. Kapuscinski, Z. Darzynkiewicz, and M. R. Melamed, "Luminescence of the Solid Complexes of Acridine Orange with RNA," vol. 2, no. 4, 1982.

[7] A. Pierzyńska-Mach, P. A. Janowski, and J. W. Dobrucki, "Evaluation of acridine orange, LysoTracker Red, and quinacrine as fluorescent probes for long-term tracking of acidic vesicles," *Cytom. Part A*, vol. 85, no. 8, pp. 729–737, 2014, doi: 10.1002/cyto.a.22495.

[8] J. Delic, J. Coppey, H. Magdelenat, and M. Coppey-Moisan, "Impossibility of acridine orange intercalation in nuclear DNA of the living cell," *Exp. Cell Res.*, vol. 194, no. 1, pp. 147–153, 1991, doi: 10.1016/0014-4827(91)90144-J.

[9] J. R. Plemel *et al.*, "Unique spectral signatures of the nucleic acid dye acridine orange can distinguish cell death by apoptosis and necroptosis," *J. Cell Biol.*, vol. 216, no. 4, pp. 1163–1181, 2017, doi: 10.1083/jcb.201602028.

[10] M. P. Thomé *et al.*, "Ratiometric analysis of Acridine Orange staining in the study of acidic organelles and autophagy," *J. Cell Sci.*, vol. 129, no. 24, pp. 4622–4632, 2016, doi: 10.1242/jcs.195057.

[11] K. O. Hubenko *et al.*, "Excimer Emission of Acridine Orange Adsorbed on Gadolinium-Yttrium Orthovanadate Nanoparticles," *J. Fluoresc.*, vol. 28, no. 4, pp. 943–949, 2018, doi: 10.1007/s10895-018-2257-9.

[12] L. Malacrida and E. Gratton, "LAURDAN fluorescence and phasor plots reveal the effects of a H2O2 bolus in NIH-3T3 fibroblast membranes dynamics and hydration," *Free Radic. Biol. Med.*, vol. 128, pp. 144–156, 2018, doi: 10.1016/j.freeradbiomed.2018.06.004.

[13] F. Fereidouni, A. N. Bader, and H. C. Gerritsen, "Spectral phasor analysis allows rapid and reliable unmixing of fluorescence microscopy spectral images," *Opt. Express*, vol. 20, no. 12, p. 12729, 2012, doi: 10.1364/oe.20.012729.

[14] B. Torrado, L. Malacrida, and S. Ranjit, "Linear Combination Properties of the Phasor Space in Fluorescence Imaging," *Sensors*, vol. 22, no. 3, 2022, doi: 10.3390/s22030999.

[15] I. Vorontsova *et al.*, "In vivo macromolecular crowding is differentially modulated by aquaporin 0 in zebrafish lens: Insights from a nanoenvironment sensor and spectral imaging," *Sci. Adv.*, vol. 8, no. 7, pp. 1–13, 2022, doi: 10.1126/sciadv.abj4833.

[16] S. Otaiza-González *et al.*, "The innards of the cell: studies of water dipolar relaxation using the ACDAN fluorescent probe," *Methods Appl Fluoresc*, vol. 10, no. 4, p. 044010, 2022, doi: 10.1088/2050-6120/ac8d4c.

[17] P. Lepanto *et al.*, "Spectral phasor analysis allows rapid and reliable unmixing of fluorescence microscopy spectral images," *Https://Doi.Org/10.6084/M9.Figshare.19469828.V1*, vol. 1232, no. Xxxx, pp. 1–

14, 2021, doi: 10.1242/bio.058734.

[18] V. Castro-Castillo *et al.*, "CAPRYDAA, an anthracene dye analog to LAURDAN: a comparative study using cuvette and microscopy," *Physiol. Behav.*, vol. 8, no. 1, pp. 88–99, 2020, doi: 10.1039/c9tb01738k.CAPRYDAA.

[19] F. Sena, M. Sotelo-Silveira, S. Astrada, M. A. Botella, L. Malacrida, and O. Borsani, "Spectral phasor analysis reveals altered membrane order and function of root hair cells in Arabidopsis dry2/sqe1-5 drought hypersensitive mutant," *Plant Physiol. Biochem.*, vol. 119, pp. 224–231, 2017, doi: 10.1016/j.plaphy.2017.08.017.

[20] L. Malacrida, S. Astrada, A. Briva, M. Bollati-Fogolín, E. Gratton, and L. A. Bagatolli, "Spectral phasor analysis of LAURDAN fluorescence in live A549 lung cells to study the hydration and time evolution of intracellular lamellar body-like structures," *Biochim. Biophys. Acta - Biomembr.*, vol. 1858, no. 11, pp. 2625–2635, 2016, doi: 10.1016/j.bbamem.2016.07.017.

[21] M. Díaz and L. Malacrida, *Advanced Fluorescence Microscopy Methods to Study Dynamics of Fluorescent Proteins In Vivo*, Vol 2564. New York, NY: Humana, 2023. doi: https://doi.org/10.1007/978-1-0716-2667-2_3.

[22] J. Schindelin *et al.*, "Fiji - an Open platform for biological image analysis," *Nat. Methods*, vol. 9, no. 7, 2012, doi: 10.1038/nmeth.2019.Fiji.

[23] S. Ranjit *et al.*, "Measuring the effect of a Western diet on liver tissue architecture by FLIM autofluorescence and harmonic generation microscopy," *Biomed. Opt. Express*, vol. 8, no. 7, p. 3143, 2017, doi: 10.1364/boe.8.003143.

[24] E. G. Suman Ranjit, Leonel Malacrida, Milka Stakic, "Determination of the metabolic index using the fluorescence lifetime of free and bound NADH in the phasor approach.," *Biophotonics*, vol. 12, no. 1, pp. 139–148, 2019, doi: 10.1002/jbio.201900156.Determination.

[25] M. Postma and J. Goedhart, "Plotsofdata—a web app for visualizing data together with their summaries," *PLoS Biol.*, vol. 17, no. 3, pp. 1–8, 2019, doi: 10.1371/journal.pbio.3000202.

[26] H. P. Mhejabeen Sayed, Bhavana Krishnamurthy, "Unraveling multiple binding modes of acridine orange to DNA using a multispectroscopic approach.," *PCCP [Phys Chem Chem Phys]*, vol. 18, no. 35, pp. 24642–53, 2016, [Online]. Available: doi:%0A10.1039/c6cp03716j

[27] A. M. Amado, W. M. Pazin, A. S. Ito, V. A. Kuzmin, and I. E. Borissevitch, "Acridine orange interaction with DNA: Effect of ionic strength," *Biochim. Biophys. Acta - Gen. Subj.*, vol. 1861, no. 4, pp. 900–909, 2017, doi: 10.1016/j.bbagen.2017.01.023.

[28] J. Kapuscinski and Z. Darzynkiewicz, "Interactions of acridine orange with double stranded nucleic acids. Spectral and affinity studies," *J. Biomol. Struct. Dyn.*, vol. 5, no. 1, pp. 127–143, 1987, doi: 10.1080/07391102.1987.10506381.

[29] A. Fucic, T. Maric, V. Vicic Bockor, and D. Jezek, "In vivo acridine orange human spermatozoa staining—A new perspective for RNA detection and spermatozoa morphology evaluation," *J. Vet. Med. Ser. C Anat. Histol. Embryol.*, vol. 50, no. 1, pp. 102–107, 2021, doi: 10.1111/ahe.12606.

[30] D. M. Damas-Souza, R. Nunes, and H. F. Carvalho, "An improved acridine orange staining of DNA/RNA," *Acta Histochem.*, vol. 121, no. 4, pp. 450–454, 2019, doi: 10.1016/j.acthis.2019.03.010.

[31] M. M. Murad, “Fluorescence Analysis of Acridine Orange Adsorbate at the Water/N-Heptane Interface, Bulk and Interface,” *J. Fluoresc.*, vol. 9, no. 3, pp. 257–263, 1999, doi: 10.1023/A:1022567919705.

[32] C. L. Riggs, N. Kedersha, P. Ivanov, and P. Anderson, “Mammalian stress granules and P bodies at a glance,” *J. Cell Sci.*, vol. 133, no. 16, pp. 1–9, 2020, doi: 10.1242/jcs.242487.

[33] E. R. Abels and X. O. Breakefield, “Introduction to Extracellular Vesicles: Bogenesis, RNA Cargo Selection, Content, Release, and Uptake,” *Cell Mol Neurobiol*, vol. 36, no. 3, pp. 301–312, 2016, doi: 10.1053/j.gastro.2016.08.014.CagY.

[34] D. S. W. Protter and R. Parker, “Principles and Properties of Stress Granules,” *Trends Cell Biol.*, vol. 26, no. 9, pp. 668–679, 2016, doi: 10.1016/j.tcb.2016.05.004.

Figure Legend

Figure 1: In vitro spectral phasor (SP) plot characterization of AO interaction with DNA and RNA solutions. A: SP of AO in three solutions where three components were determined. Magenta cursor marks AO fully bound (Fb) to RNA, green cursor AO Fb to DNA and cyan cursor free AO. B: Average intensity and pseudo-color images of AO solutions in A showing the best fit of cursors position in the center of mass from data distribution. In the bottom part there is a spectral plot of the images from the three solutions. C and D: Zoomed-in phasor plots showing two trajectories and partially bound (Pb) or Fb of AO to DNA (C) or RNA (D). The right graphs represent the normalized number of pixels from the left images as a function of the DNA or RNA AO-bound fraction. DNA Pb: 0.1 mg/ml, RNA Pb: 0.7 mg/ml.

Figure 2: Basic spectral and phasor plot analysis of hyperspectral confocal images from NIH-3T3 AO-stained fixed cells. A: Spectral acquisition of 22 channels from 503 to 723 nm by confocal microscopy. The hyperspectral image was obtained by the sum of all the spectral images obtained in steps of 10 nm. Magenta region of interest (ROI) was placed on the cytoplasm and cyan ROI on the nucleus. The graph on the right shows the mean spectral curves from both ROIs, as normalized intensity vs. wavelength. B: Left, average intensity image of a cell segmented from the image in A. The spectral phasor plot of this representative cell is shown in the middle. Right, pseudo-color image showing the cellular regions enriched in AO bound to RNA (magenta) or DNA (green). Cursors in the phasor plot are placed on the positions previously determined with solutions in figure 1. Scale bar: 10 µm.

Figure 3: Two-component spectral phasor plot analysis of hyperspectral images of whole and segmented fixed NIH-3T3 cells stained with AO. A: Phasor plot of a representative cell. The dimension AO bound to DNA or RNA was analyzed and the cluster of pixels is projected in the trajectory indicated by the black line. Upper color scale and the pseudo-color image on the right represent the proportion of pixels in the trajectory for the different fractions of AO bound to DNA or RNA. The pixels with the highest proportion of AO bound to DNA are shown in red and those with the highest proportion of AO bound to RNA are shown in blue. B: Histograms of normalized number of pixels as a function of the AO-DNA fraction. Ten cells were analyzed (each cell represented by a color curve) and the mean curve in black +SD shows that 50 % of pixels in the images are of AO bound to DNA. C and D: Spectral phasor plot analysis of the segmented nucleus (C) and cytoplasm (D). Example inserted pseudo-color images are from the cell in A. Histograms of fraction indicate the distribution of AO bound to DNA and RNA. E: Center of mass violin plots showing the different proportions and distribution of AO bound to DNA in nucleus and cytoplasm. Wilcoxon matched-pairs test, ***p=0.0005. N= 10. Scale bar 10 µm.

Figure 4: Basic spectral and phasor plot analysis of hyperspectral images of NIH-3T3 live cells stained with AO. A: The hyperspectral confocal image, represented as the sum of

22 channels shows two selected regions of interest (ROIs) placed on the nucleus (cyan) and the cytoplasm (magenta). The graph on the right displays the average AO spectra from these ROIs. B: Left (image 1) and center (image 2), maximum average intensity projections were generated splitting in two the original lambda stack in A. A merge is shown on the right (green, image 1; magenta, image 2). C: Center, spectral phasor plot of the live cell, where 3 regions are identified. In addition to the components AO bound to RNA (magenta) and DNA (green), a third component appears (C_3). Pixels that have linear combinations with C_3 appear colored in cyan in the pseudo-color image on the right. Scale bar 10 µm.

Figure 5: Three components spectral phasor plot analysis of living NIH-3T3 cells stained with AO. A: In this phasor plot of a representative live cell, a three-component analysis was performed, and two dimensions analyzed. In the first dimension all the pixels are projected in the linear combination between AO bound to DNA or RNA, in the second dimension the pixels are projected in the linear combination between AO bound to DNA or the third component (C_3). The right pseudo-color images and color scales show the distribution and proportion of the different components inside the live cell in both dimensions. B: Histograms of normalized number of pixels as a function of the fraction in percentage of AO bound to DNA or C_3. Fifteen cells were processed, and mean curves with SD are shown in black. C and D: Three components analysis phasor plot of segmented nuclei (C) and cytoplasm (D) of live cells. Inserted pseudo-color images are taken from the cell in A, mean curves, and SD of histograms of component fractions indicate the proportion of AO bound to the three components inside live cells. E: Center of mass violin plots showing the different proportions and distribution of AO bound to DNA or C_3 in nucleus and cytoplasm. Wilcoxon matched-pairs test, ****$p<0.0001$. N=15. Scale bar 10 µm.

Figure 6: Characterization of the third component (C_3) of AO in live NIH-3T3 cells. A: Brightfield image. B - D: Maximum intensity projections of spectral confocal images of cells stained with AO and LysoTracker Deep Red deep red (Ex: 647 nm). Th original lambda stack was separated into three channels, image B, C and D. E: Merge image of the three channels. Green: AO Ch 1, magenta: AO Ch 2 and Cyan: LysoTracker. Magnified region shows Cyan-magenta spots that represent acidic structures co-stained with AO and LysoTracker Deep Red. F: Spectral phasor plot of a live cell stained with LysoTracker Deep Red. The red cursor marks the cluster of data correlated with lysosome-like spots in the average intensity image inserted. G: Spectral phasor plot of live cell stained with AO and LysoTracker Deep Red. The yellow area encloses a cluster of data that correspond to pixels with a linear combination of AO bound to RNA, DNA and C_3 stained with LysoTracker Deep Red. The magenta area encloses pixels with a linear combination between component AO-RNA and C_3 but no with LysoTracker Deep Red. The average intensity image inserted in this plot, obtained with phasor analysis, correlates yellow and magenta areas with magenta and cyan areas of figure E. Scale bar 10 µm.

Figure 1

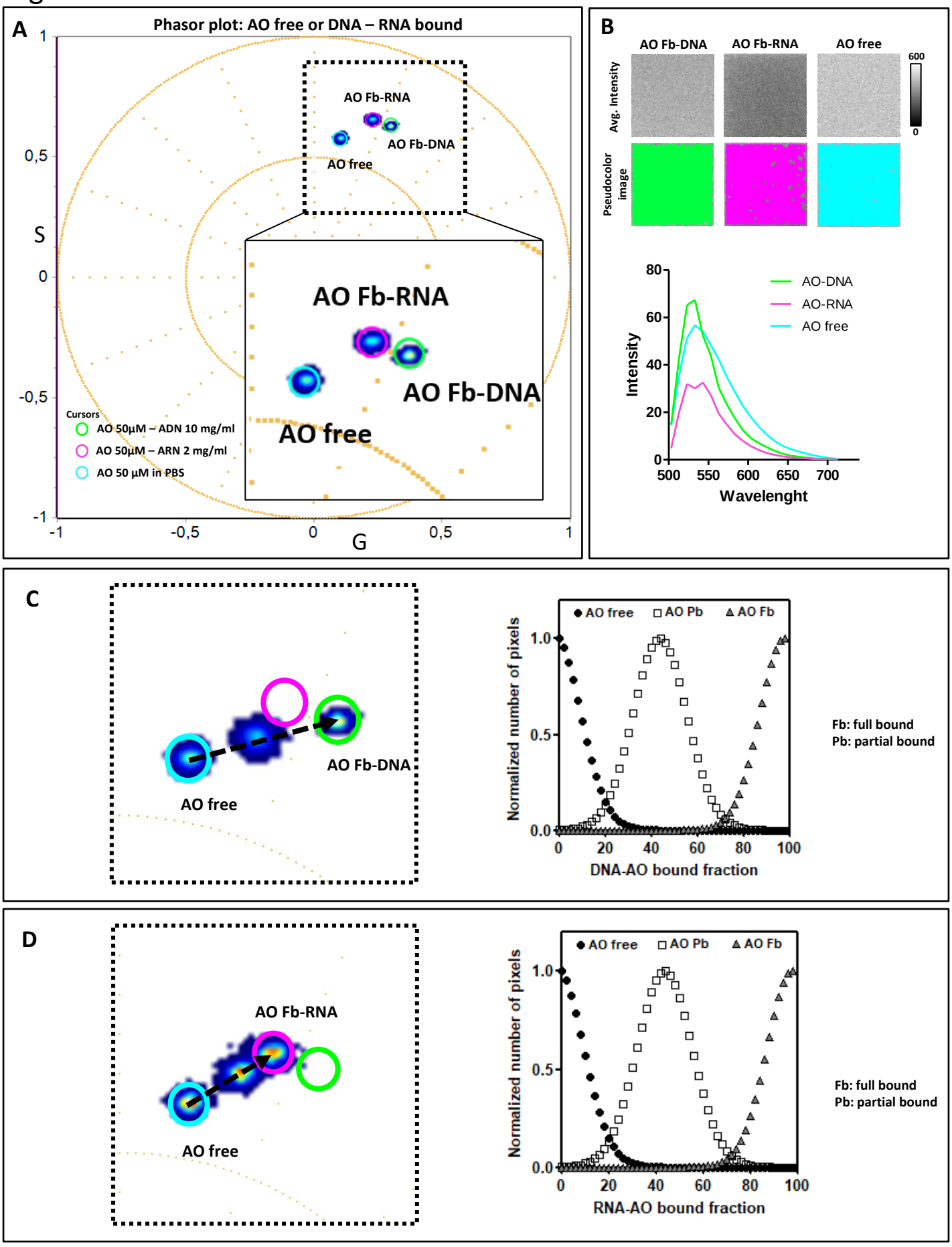
A
Phasor plot: AO free or DNA – RNA bound
AO Fb-RNA
AO Fb-DNA
AO free
S
G
Cursors
AO 50µM – ADN 10 mg/ml
AO 50µM – ARN 2 mg/ml
AO 50 µM in PBS
B
AO Fb-DNA
AO Fb-RNA
AO free
Avg. Intensity
Pseudocolor image
600
0
AO-DNA
AO-RNA
AO free
Intensity
Wavelenght
C
AO Fb-DNA
AO free
AO free
AO Pb
AO Fb
Normalized number of pixels
DNA-AO bound fraction
Fb: full bound
Pb: partial bound
D
AO Fb-RNA
AO free
AO free
AO Pb
AO Fb
Normalized number of pixels
RNA-AO bound fraction
Fb: full bound
Pb: partial bound

Figure 2

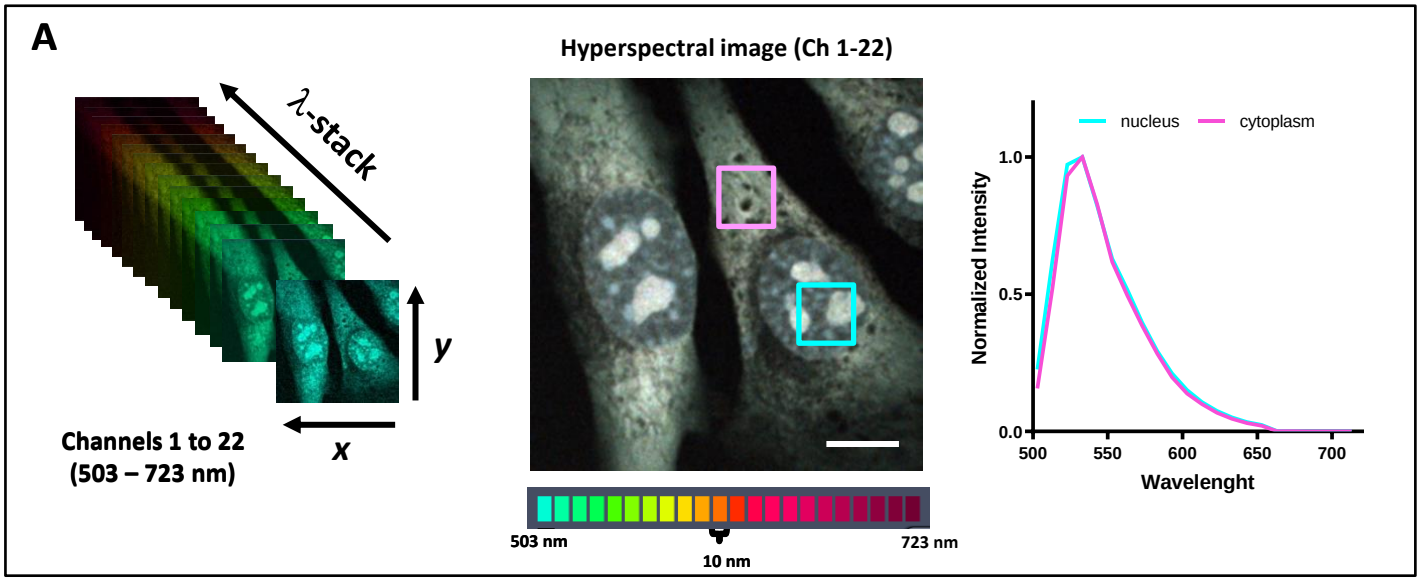
A
λ-stack
y
x
Channels 1 to 22
(503 – 723 nm)
Hyperspectral image (Ch 1-22)
503 nm
10 nm
723 nm
nucleus
cytoplasm
Normalized Intensity
1.0
0.5
0.0
500
550
600
650
700
Wavelenght

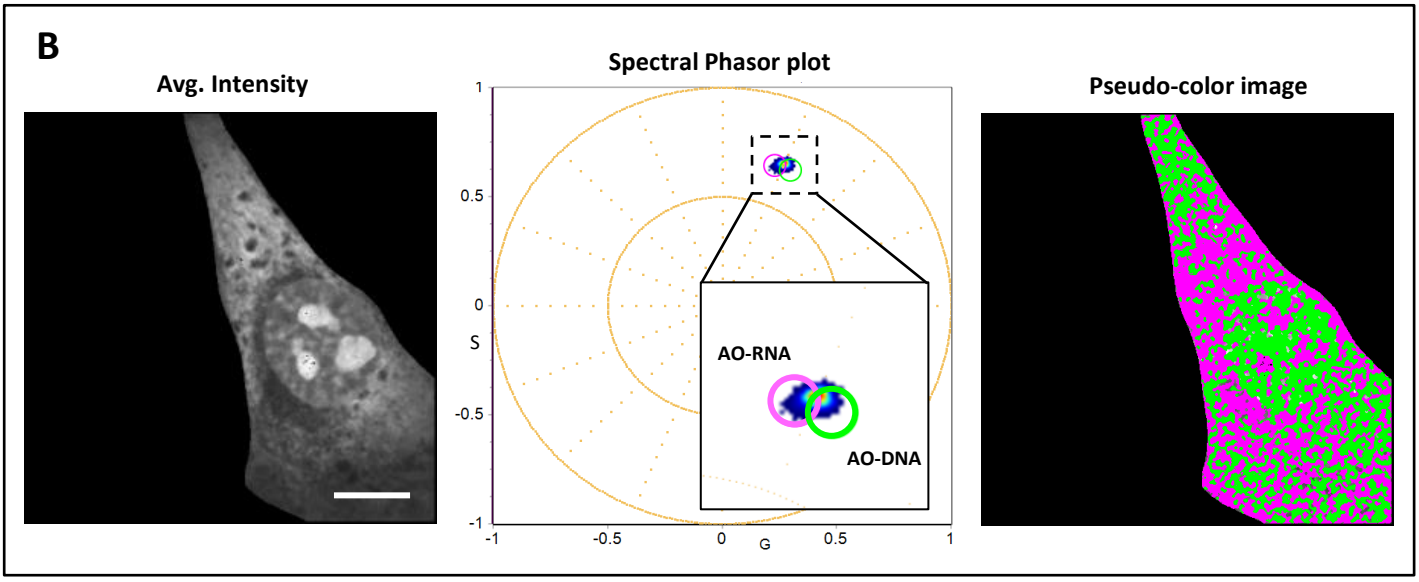
B
Avg. Intensity
Spectral Phasor plot
Pseudo-color image
AO-RNA
AO-DNA
S
G
1
0.5
0
-0.5
-1

Figure 3

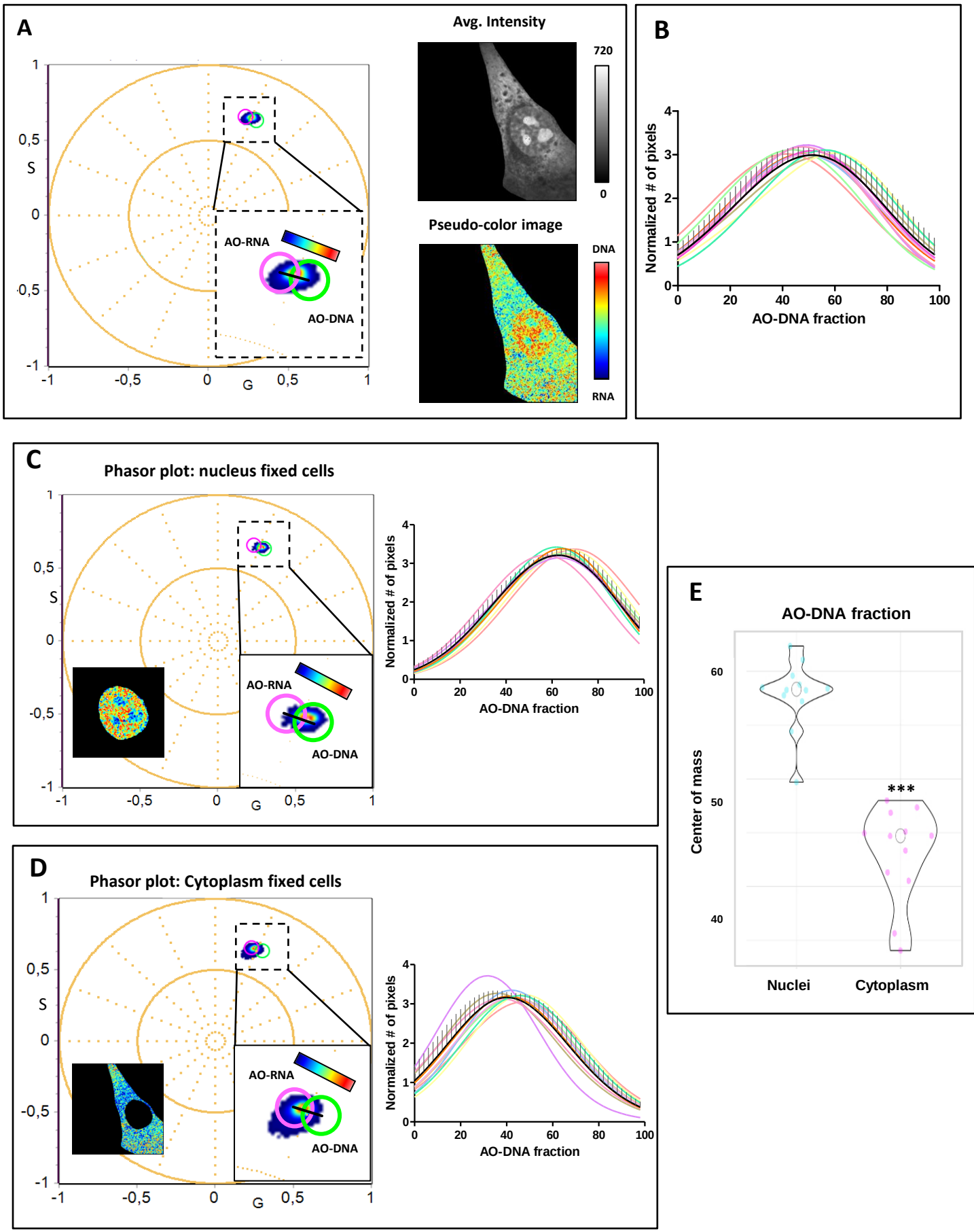
A
Avg. Intensity
720
0
Pseudo-color image
DNA
RNA
AO-RNA
AO-DNA
S
G
B
Normalized # of pixels
AO-DNA fraction
C
Phasor plot: nucleus fixed cells
D
Phasor plot: Cytoplasm fixed cells
E
AO-DNA fraction
Center of mass
***
Nuclei
Cytoplasm

Figure 4

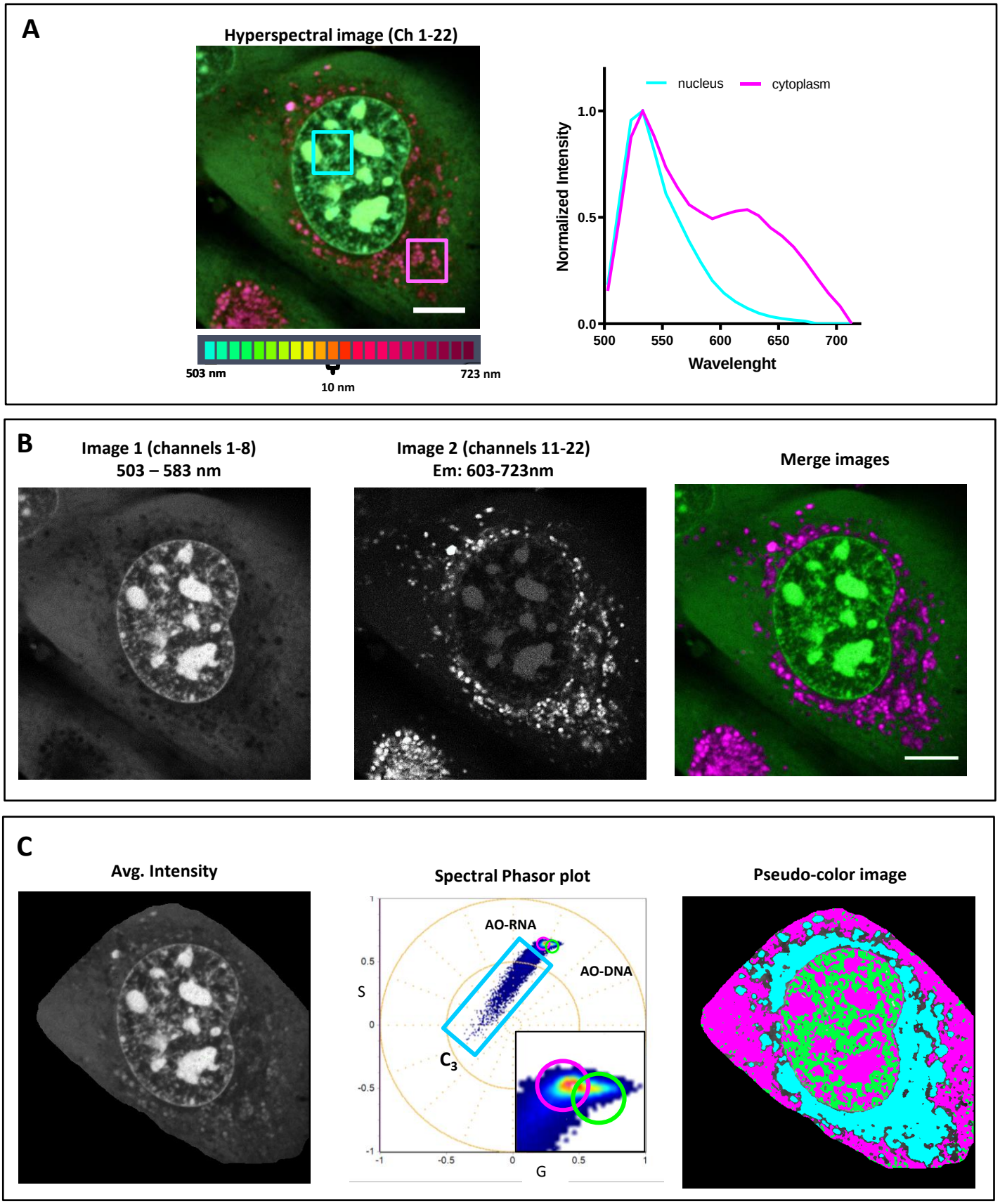
A
Hyperspectral image (Ch 1-22)
503 nm
10 nm
723 nm
nucleus
cytoplasm
Normalized Intensity
1.0
0.5
0.0
500
550
600
650
700
Wavelenght
B
Image 1 (channels 1-8)
503 – 583 nm
Image 2 (channels 11-22)
Em: 603-723nm
Merge images
C
Avg. Intensity
Spectral Phasor plot
Pseudo-color image
AO-RNA
AO-DNA
S
G
C3
0.5
0
-0.5
-1
1

Figure 5

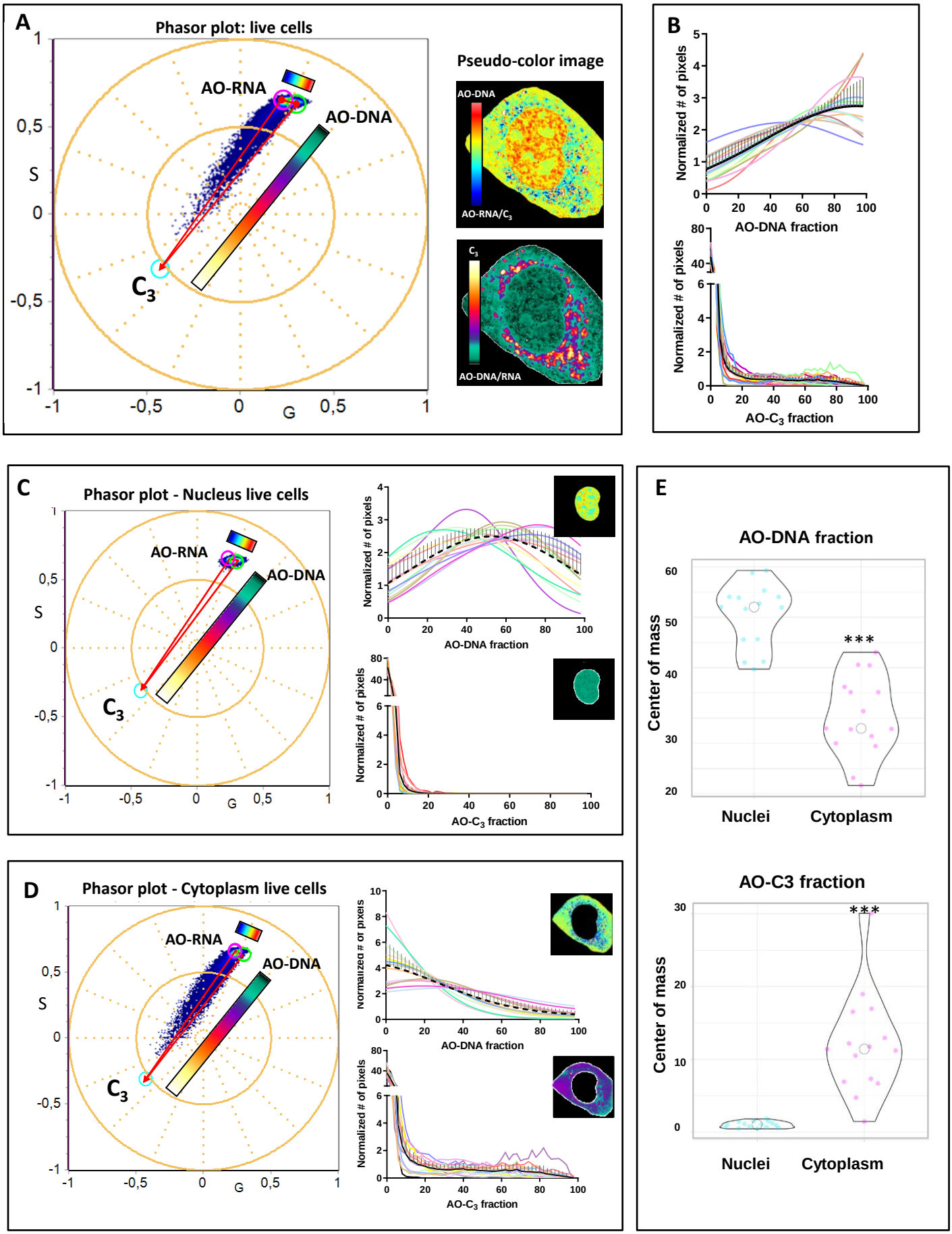
A
Phasor plot: live cells
AO-RNA
AO-DNA
C3
S
G
Pseudo-color image
AO-DNA
AO-RNA/C3
C3
AO-DNA/RNA
B
Normalized # of pixels
AO-DNA fraction
AO-C3 fraction
C
Phasor plot - Nucleus live cells
D
Phasor plot - Cytoplasm live cells
E
AO-DNA fraction
Center of mass
***
Nuclei
Cytoplasm
AO-C3 fraction

Figure 6

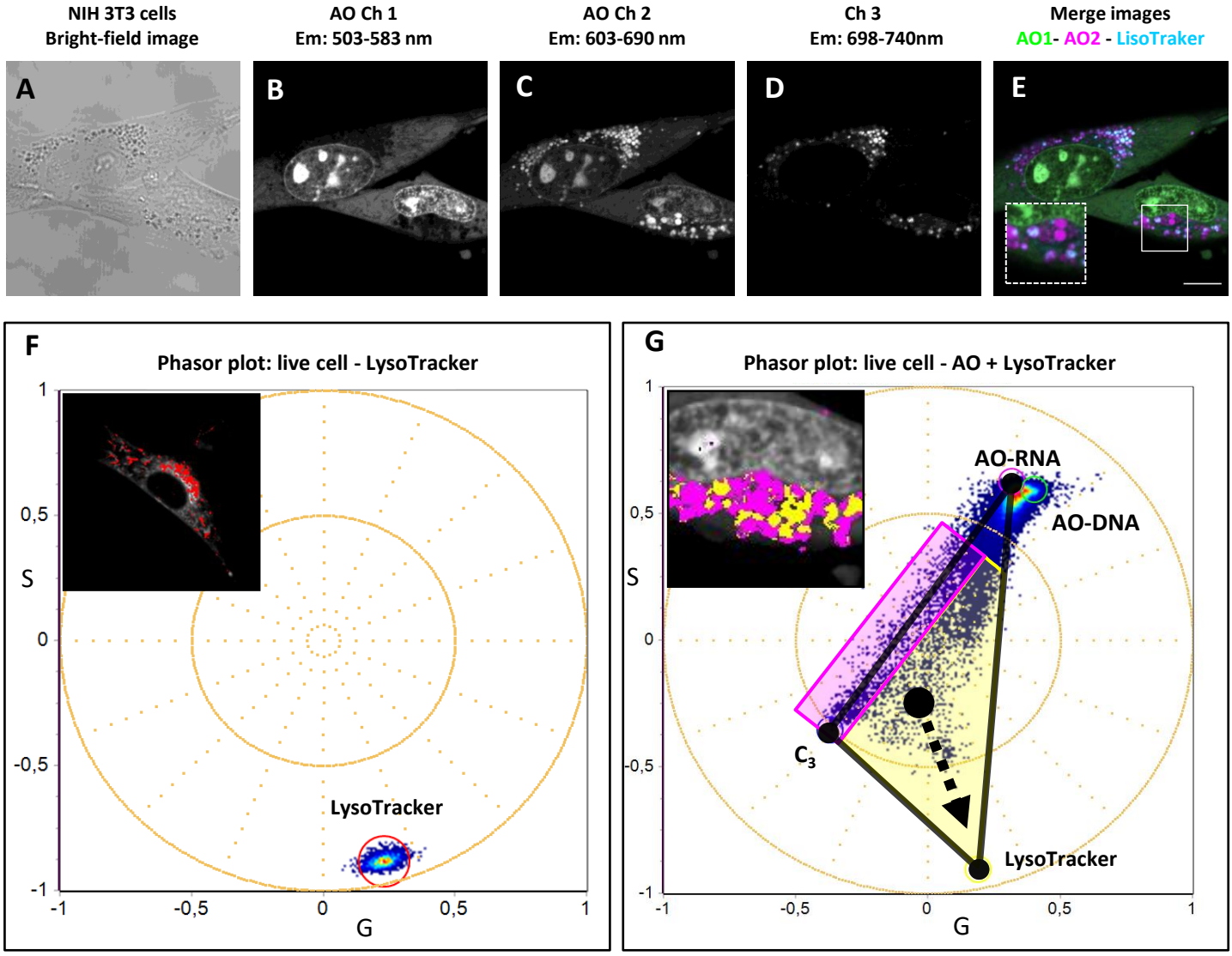
NIH 3T3 cells
Bright-field image
AO Ch 1
Em: 503-583 nm
AO Ch 2
Em: 603-690 nm
Ch 3
Em: 698-740nm
Merge images
AO1- AO2 - LisoTraker
A
B
C
D
E
F
Phasor plot: live cell - LysoTracker
LysoTracker
S
G
G
Phasor plot: live cell - AO + LysoTracker
AO-RNA
AO-DNA
C3
LysoTracker
S
G